

# Boron-Based Functional Additives Enable Solid Electrolyte Interphase Engineering in Calcium Metal Battery

Charlotte Bodin<sup>[a, h]</sup>, Juan Forero Saboya<sup>[a]</sup>, Piotr Jankowski,<sup>[b, c]</sup> Kristian Radan,<sup>[d]</sup> Dominique Foix,<sup>[e, i]</sup> Cécile Courrèges,<sup>[e, i]</sup> Ibraheem Yousef,<sup>[f]</sup> Rémi Dedryvère,<sup>[e, h, i]</sup> Carine Davoisne,<sup>[g, h, i]</sup> Matic Lozinšek,<sup>\*[d]</sup> and Alexandre Ponrouch<sup>\*[a, h]</sup>

Calcium-metal batteries have received growing attention recently after several studies reporting successful metal plating and stripping with organic electrolytes. Given the low redox potential of metallic calcium, its surface is commonly covered by a passivation layer grown by the accumulation of electrolyte decomposition products. The presence of borate species in this layer has been shown to be a key parameter allowing for  $\text{Ca}^{2+}$  migration and favoring Ca electrodeposition. Here, boron-based additives are evaluated in order to tune the SEI composition,

morphology, and properties. The decomposition of a  $\text{BF}_3$ -based additive is studied at different potentiostatic steps and the resulting SEI layer was thoroughly characterized. SEI growth mechanism is proposed based on both experimental data and DFT calculations pointing at the formation of boron-crosslinked polymeric matrices. Several boron-based adducts are explored as SEI-forming additives for calcium-metal batteries paving the way to very rich chemistry leading to  $\text{Ca}^{2+}$  conducting SEI.

## Introduction

Among the different post-Li batteries, calcium-metal batteries are the object of growing interest due to the abundance of raw materials and interesting electrochemical characteristics such as a low standard redox potential ( $-2.87 \text{ V}$  vs. SHE) and a high theoretical specific capacity ( $1340 \text{ mAh g}^{-1}$ ). The feasibility of calcium plating and stripping on a metallic calcium electrode has first been demonstrated using a  $\text{Ca}(\text{BF}_4)_2$  electrolyte in a carbonate solvent, at moderate temperatures,<sup>[1]</sup> which later was also suggested to occur at room temperature.<sup>[2]</sup> Since then, other electrolyte formulations have been reported, allowing for the operation of the metal negative electrode at room temper-

ature. For example, employing  $\text{Ca}(\text{BH}_4)_2$  in tetrahydrofuran,<sup>[3]</sup> alkoxyborate calcium salts in dimethoxyethane,<sup>[4,5]</sup> and more recently the first use of an alkoxyaluminate calcium salt in the same solvent.<sup>[6]</sup> Additionally, the use of ionic liquids as electrolytes for calcium plating has been reported.<sup>[7]</sup> The increase number of reports demonstrating calcium plating has encouraged the study of the effects of the substrate and the cation solvation shell in the kinetics of electrodeposition.<sup>[8]</sup>

Given the low redox potential of metallic calcium, the surface of the electrode is often covered by a passivation layer, formed by electrolyte decomposition products. In order to optimize the plating/stripping reactions at the electrode, it is crucial to understand the formation mechanism of this layer,

[a] Dr. C. Bodin,\* Dr. J. Forero Saboya,\* Dr. A. Ponrouch  
Institut de Ciència de Materials de Barcelona, ICMAB-CSIC  
Campus UAB  
08193, Bellaterra, Spain  
E-mail: aponrouch@icmab.es

[b] Dr. P. Jankowski  
Department of Energy Conversion and Storage  
Technical University of Denmark  
Kgs. Lyngby, 2800, Denmark

[c] Dr. P. Jankowski  
Faculty of Chemistry  
Warsaw University of Technology  
00-661 Warsaw, Poland

[d] Dr. K. Radan, Dr. M. Lozinšek  
Department of Inorganic Chemistry and Technology, Jožef Stefan Institute  
Jamova Cesta 39  
1000, Ljubljana, Slovenia  
E-mail: matic.lozinsek@ijs.si

[e] Dr. D. Foix, Dr. C. Courrèges, Prof. R. Dedryvère  
IPREM, E2S-UPPA, CNRS, Université de Pau & Pays de l'Adour  
2, av. du Président Angot  
64053, Pau, France

[f] Dr. I. Yousef  
MIRAS Beamline, ALBA Synchrotron Light Source  
Carrer de la Llum 2-26  
08290, Cerdanyola del Vallès, Spain

[g] Dr. C. Davoisne  
Laboratoire de Réactivité et Chimie des Solides  
Université de Picardie Jules Verne, CNRS UMR7314  
15 rue Baudelocque  
80039 Amiens Cedex 1, France

[h] Dr. C. Bodin,\* Prof. R. Dedryvère, Dr. C. Davoisne, Dr. A. Ponrouch  
ALISTORE – European Research Institute – CNRS FR 3104, 15 rue Baudelocque  
80039 Amiens Cedex 1, France

[i] Dr. D. Foix, Dr. C. Courrèges, Prof. R. Dedryvère, Dr. C. Davoisne  
RS2E, Réseau Français sur le Stockage Electrochimique de l'Energie, FR CNRS  
3459, 15 rue Baudelocque  
80039 Amiens Cedex 1, France

[\*] These authors contributed equally to this work.

 Supporting information for this article is available on the WWW under <https://doi.org/10.1002/batt.202200433>

 © 2022 The Authors. *Batteries & Supercaps* published by Wiley-VCH GmbH. This is an open access article under the terms of the Creative Commons Attribution Non-Commercial License, which permits use, distribution and reproduction in any medium, provided the original work is properly cited and is not used for commercial purposes.

and identify possible components allowing for  $\text{Ca}^{2+}$  migration. However, there are only few studies in the literature devoted to the understanding of this passivation layer formation, as pointed out in recent review articles.<sup>[9,10]</sup>

Previously, our group has studied the passivation layer formed in either  $\text{Ca}(\text{BF}_4)_2$  or  $\text{Ca}(\text{TFSI})_2$ -based electrolytes.<sup>[11]</sup> It was noted that such layer formed with the  $\text{Ca}(\text{BF}_4)_2$  salt is permeable to calcium cations, thus behaving as a solid electrolyte interphase (SEI), while the one formed with the  $\text{Ca}(\text{TFSI})_2$  salt is ionically blocking. This beneficial behavior of the  $\text{Ca}(\text{BF}_4)_2$ -related SEI was attributed to the presence of boron-containing (not well-defined) species. An alternative route to include boron species in the passivation layer is the use of functional electrolyte additives. The use of boron trifluoride,  $\text{BF}_3$  (stabilized in diethyl ether, i.e.,  $\text{BF}_3\cdot\text{DE}$ ), as an additive to a  $\text{Ca}(\text{TFSI})_2$ -based electrolyte has been previously reported to allow for calcium plating and stripping with comparable kinetics as when using a  $\text{Ca}(\text{BF}_4)_2$ -based electrolyte.<sup>[12]</sup> Although the kinetics of Ca plating/stripping in this electrolyte are still low compared to the alkoxyborate electrolytes mentioned before, the  $\text{Ca}^{2+}$  conductive nature of the SEI is expected to open the road for better SEI-engineering or artificial SEI development in calcium-metal and other divalent batteries.

The use of such  $\text{BF}_3$  complexes is not restrained to calcium ion batteries. In the case of lithium-ion, a decrease of the overall resistance and an increase of the cycle life of  $\text{Li}[\text{Ni}_{0.33}\text{Co}_{0.33}\text{Mn}_{0.33}\text{O}_2]/\text{graphite}$  full cells were observed when  $\text{BF}_3$  complexes are included as electrolyte additives.<sup>[13]</sup> The presence of the additive was hypothesized to influence the passivation/decomposition reactions that occur at one or both electrode surfaces. However, no clear evidence of such influence was provided aside from the presence of boron species at the surface of the electrodes. A better understanding of the beneficial action of this additive is needed to optimize the use of boron-based additives in lithium-ion as well as in next-generation batteries and to clarify the nature of SEI components allowing for  $\text{Ca}^{2+}$  migration.

In this work, we investigate the composition and morphology of the SEI formed with  $\text{BF}_3\cdot\text{DE}$  after polarization of the Ca electrode at different potentials, through transmission electron microscopy (TEM), electron energy loss spectroscopy (EELS), X-ray photoelectron spectroscopy (XPS), time-of-flight secondary ion mass spectrometry (ToF-SIMS) and synchrotron-based Fourier-transform infrared (SR-FTIR) microspectroscopy measurements. The impact of different cut-off potentials on the composition and morphology of the passivation layer is studied. In particular, the inclusion of boron-containing species and the feasibility of reversible Ca plating are described. To understand the mechanisms leading to this SEI composition, the formation of  $\text{BF}_3$  complexes in solution, and their degradation upon reduction were investigated by DFT calculations.

## Results and Discussion

### Influence of the SEI layer on the calcium electrodeposition

The feasibility of calcium plating/stripping from a  $\text{Ca}(\text{TFSI})_2$ -based electrolyte has been previously demonstrated by the addition of  $\text{BF}_3\cdot\text{DE}$ .<sup>[12]</sup> As the electrochemical behavior is similar to the one observed when  $\text{Ca}(\text{BF}_4)_2$ -based electrolyte is used, the solid electrolyte interphase formed when the boron-based additive is used deserves some investigation. Here, we investigate how the composition and morphology of the passivation layer impact the Ca plating and stripping kinetics. In order to ascertain the impact of the lower cutoff potential on the formation of the passivation layer and on the Ca plating kinetics, four electrodes were pre-passivated at different potentials ( $-2.0$ ,  $-3.0$ ,  $-4.0$ , and  $-4.6$  V vs.  $\text{Ag}_{\text{QRE}}$  during 48 h) prior to cyclic voltammetry measurements. Nickel disks were used as the working electrode and thus covered by the SEI layer when polarized in a  $0.4 \text{ mol L}^{-1} \text{ Ca}(\text{TFSI})_2$  in EC:PC + 2 wt%  $\text{BF}_3\cdot\text{DE}$  electrolyte. Figure 1 summarizes the evolution of cyclic voltammograms obtained after the passivation at different potentials. In all cases, CVs were performed in the same potential range between  $-0.9$  and  $-4.6$  V vs.  $\text{Ag}_{\text{QRE}}$  which was previously found to allow for Ca plating and stripping since Ca plating is typically observed at an onset potential of about  $-3.4$  V vs.  $\text{Ag}_{\text{QRE}}$ .<sup>[12]</sup> When the substrate was pre-passivated at  $-2.0$  V vs.  $\text{Ag}_{\text{QRE}}$ , no Ca plating/stripping could be observed during the first five cycles, and barely visible for  $-3.0$  V vs.  $\text{Ag}_{\text{QRE}}$  (Figure 1) suggesting that the passivation layer formed at those potentials does not allow  $\text{Ca}^{2+}$  migration. By contrast, clear Ca stripping (oxidation) peaks were immediately recorded for substrates previously polarized at  $-4.0$  and  $-4.6$  V vs.  $\text{Ag}_{\text{QRE}}$ . After a few cycles, CVs with clear reductive and oxidative contributions for each pre-passivated sample can be observed, Figure 1(c). The evolution of the Ca stripping charge for each pre-passivation is presented in Figure 1(d) where a clear leap is visible at the fifth cycle for the  $-2.0$  V and  $-3.0$  V vs.  $\text{Ag}_{\text{QRE}}$ .

Therefore, performing plating/stripping cycles on the previously passivated substrates significantly changes the properties of the deposited layer, particularly for the layers prepared at  $-2.0$  and  $-3.0$  V vs.  $\text{Ag}_{\text{QRE}}$ . While these surface layers did not allow for calcium plating in the first cycles (the stripping charge was nil or very small), the situation gradually improves until they are comparable to the surface layers produced at  $-4.0$  and  $-4.6$  V vs.  $\text{Ag}_{\text{QRE}}$ . Additionally, when performing plating/stripping cycles using the previously deposited layer at  $-2.0$  and  $-3.0$  V vs.  $\text{Ag}_{\text{QRE}}$ , a constant reduction current is recorded suggesting that some parasitic reactions are still happening at the surface and possibly a different surface layer is being grown.

In brief, these results suggest that the passivation layers formed after a 48 h potentiostatic step are not fully stable and could evolve upon cycling, and that the potential at which this pre-passivation has been performed strongly impacts the overall evolution upon cycling of the Ca plating and stripping kinetics. Importantly, the surface layers formed at potentials below Ca metal plating (ca.  $-3.4$  V vs.  $\text{Ag}_{\text{QRE}}$ ) favor the

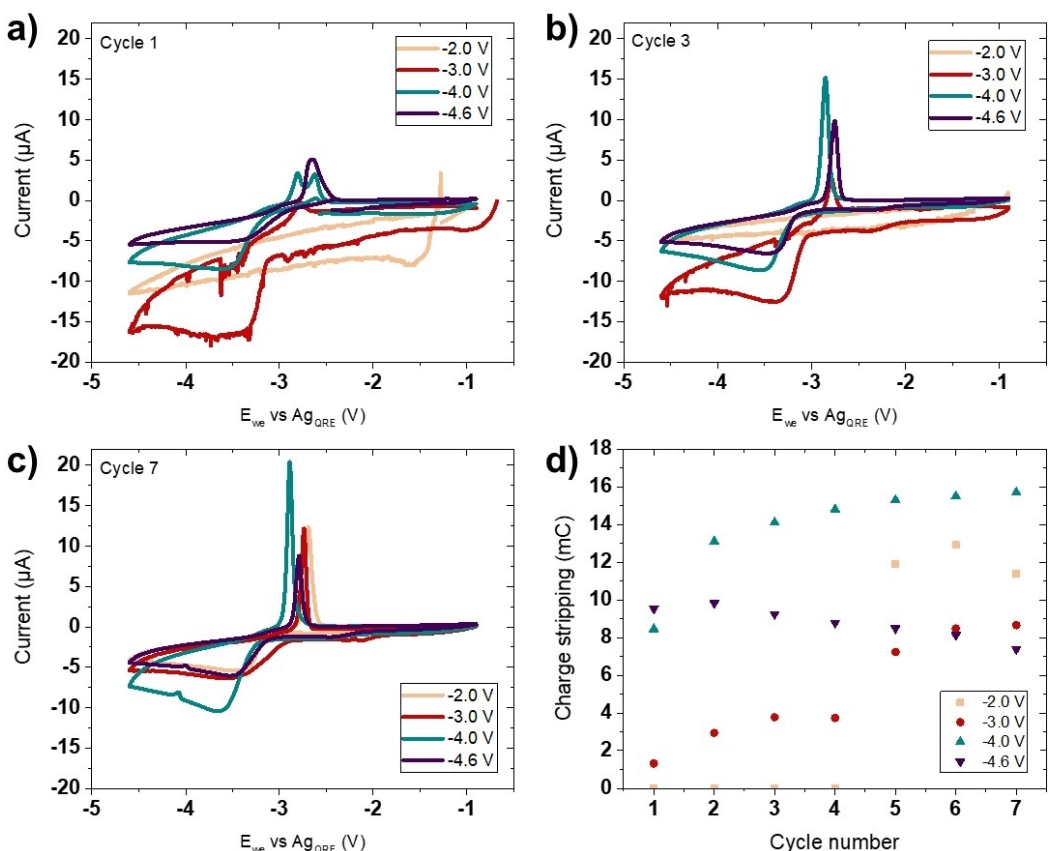


**Figure 1.** Cyclic voltammograms ( $0.4 \text{ mol L}^{-1}$   $\text{Ca}(\text{TFSI})_2$  in EC:PC with 2 wt% of  $\text{BF}_3\text{-DE}$ ,  $0.1 \text{ mVs}^{-1}$ ,  $100^\circ\text{C}$ ) after 48 h potentiostatic polarization at  $-2.0 \text{ V}$ ,  $-3.0 \text{ V}$ ,  $-4.0 \text{ V}$  and  $-4.6 \text{ V}$  vs.  $\text{Ag}_{\text{QRE}}$ : a) cycle 1, b) cycle 3, c) cycle 7 and d) the charge stripping upon cycling.

migration of cations, highlighting the importance of Ca deposition taking place during the formation of the passivation layer.

#### $\text{BF}_4^-$ vs. $\text{TFSI} + \text{BF}_3\text{-DE}$ derived SEI

The morphology of the passivation layers formed on nickel substrate was studied by transmission electron microscopy

(Figure 2). The electrolytes used were  $0.5 \text{ mol L}^{-1}$   $\text{Ca}(\text{BF}_4)_2$  in EC:PC and  $0.4 \text{ mol L}^{-1}$   $\text{Ca}(\text{TFSI})_2$  in EC:PC with and without 2 wt% of  $\text{BF}_3\text{-DE}$ . Nickel particles were polarized below  $-3.8 \text{ V}$  vs.  $\text{Ag}_{\text{QRE}}$  for 48 h at  $100^\circ\text{C}$ .<sup>[14]</sup> As discussed previously,<sup>[11]</sup> passivation layers formed in  $\text{Ca}(\text{BF}_4)_2$  based-electrolyte are relatively thick (about 100 nm) and inhomogeneous with at least two distinct microstructures (Figure 2a). The region denoted “SEI 1” has a microstructure like thin flakes (area surrounded by dash line in Figure 2a) which are amorphous and composed of

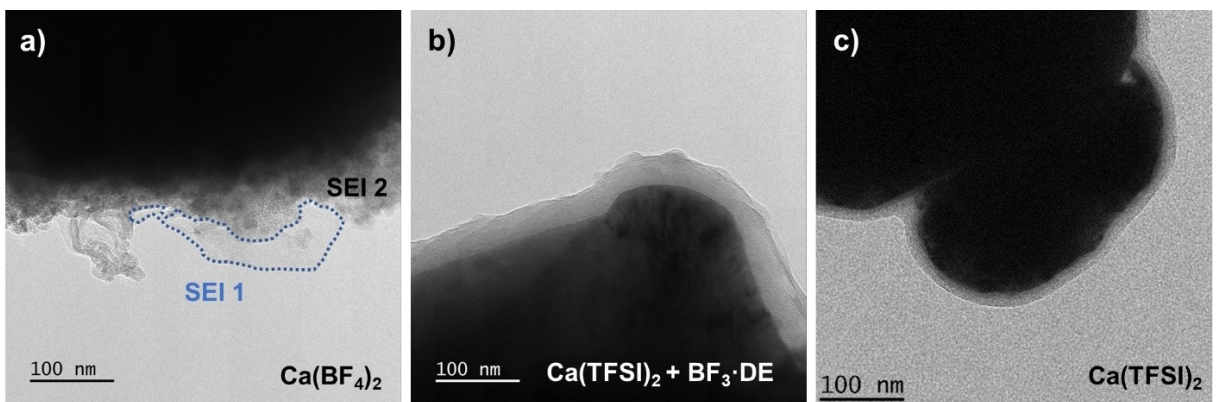


**Figure 2.** TEM images of passivated nickel particles polarized at  $100^\circ\text{C}$  for 48 h at a)  $-3.8 \text{ V}$ , and b and c)  $-4.0 \text{ V}$  vs.  $\text{Ag}_{\text{QRE}}$  with an electrolyte composed of a)  $0.5 \text{ mol L}^{-1}$   $\text{Ca}(\text{BF}_4)_2$  in EC:PC and b)  $0.4 \text{ mol L}^{-1}$   $\text{Ca}(\text{TFSI})_2$  in EC:PC with 2 wt% of  $\text{BF}_3\text{-DE}$  or c) without.

carbonaceous species and include borates, whereas, "SEI 2" is mostly constituted of agglomerates of small particles with a crystalline structure corresponding to  $\text{CaF}_2$ . A significantly different morphology was observed using electrolytes containing  $\text{Ca}(\text{TFSI})_2 + \text{BF}_3 \cdot \text{DE}$  from which an amorphous and homogeneous layer was formed (Figure 2b). Conformal uniform coatings were obtained with typical thicknesses around 40 nm. Such morphology is reminiscent of the passivation layer obtained when  $\text{Ca}(\text{TFSI})_2$  salt was used without  $\text{BF}_3$  additive (Figure 2c). The passivation layer formed with  $\text{Ca}(\text{BF}_4)_2$  and  $\text{Ca}(\text{TFSI})_2 + \text{BF}_3 \cdot \text{DE}$ -based electrolyte allowed calcium diffusion. However, in the case of  $\text{Ca}(\text{TFSI})_2$ -based electrolyte, even though the layer was thinner (< 20 nm), it was fully blocking, thus preventing Ca plating and stripping.<sup>[11]</sup>

The SEI formed with  $\text{Ca}(\text{TFSI})_2 + \text{BF}_3 \cdot \text{DE}$  was characterized in-depth by analyzing the microstructure, composition, and homogeneity with TEM, EELS, XPS, and SR-FTIR measurements.

## TFSI + $\text{BF}_3 \cdot \text{DE}$ derived SEI: influence of the applied potential

### Microstructure of the SEI

Four different passivation layers were grown by varying the applied potential ( $-2.0$ ,  $-3.0$ ,  $-4.0$ , and  $-4.6$  V vs.  $\text{Ag}_{\text{QRE}}$ ; note that Ca plating is observed in this electrolyte at around  $-3.4$  V vs.  $\text{Ag}_{\text{QRE}}$ ). Here, nickel particles were used as the working electrode and thus covered by the SEI layer when polarized in a  $0.4 \text{ mol L}^{-1}$   $\text{Ca}(\text{TFSI})_2$  in EC:PC + 2 wt%  $\text{BF}_3 \cdot \text{DE}$  electrolyte. An amorphous passivation layer was observed in all cases, yet, differences in terms of thickness and microstructure are noticeable depending on the applied potential, as shown in Figure 3. While the formed passivation layer is thinner than 30 nm at  $-2.0$  V vs.  $\text{Ag}_{\text{QRE}}$ , the layer formed at  $-4.6$  V vs.  $\text{Ag}_{\text{QRE}}$  is about 60 nm thick. The latter also presents a great number of thin flakes at the surface. In some cases, protruding polycrystalline particles were also observed on top of the amorphous passivation layer, as shown in Figure 4(a) (area 2 in red). The composition of these different microstructures was investigated locally by means of electron diffraction and EELS and an overall composition of the passivation layer was determined by XPS and SR-FTIR.

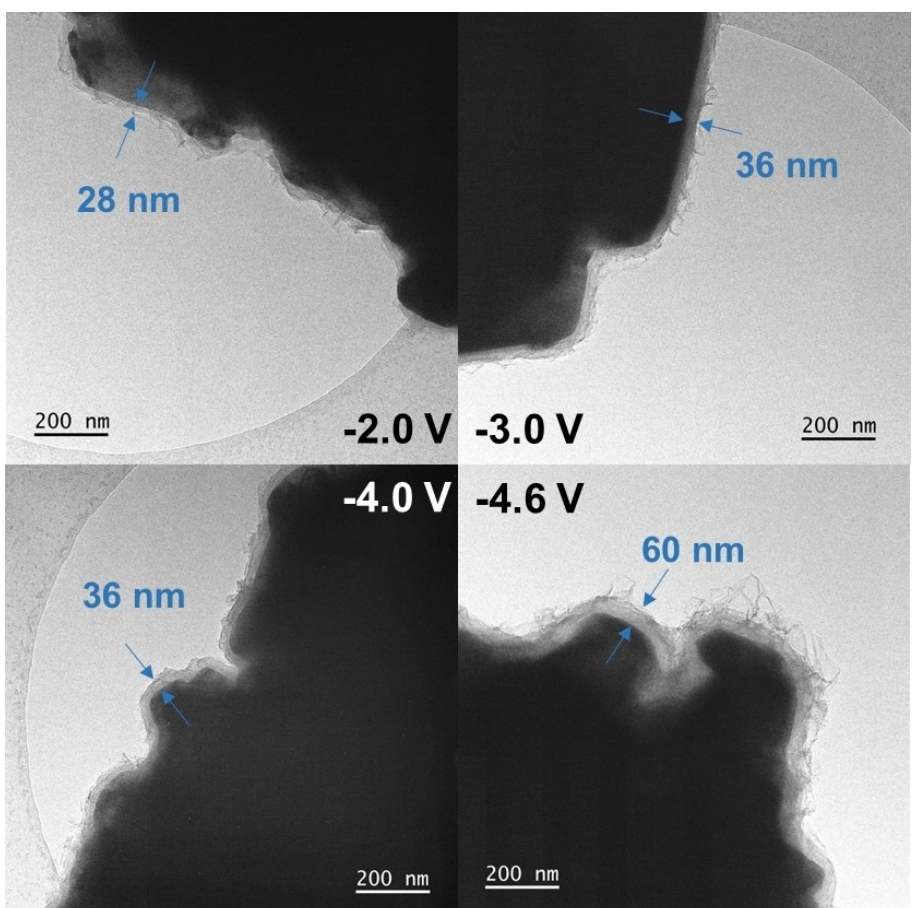


**Figure 3.** TEM images of passivation layer covered nickel particles prepared at  $-2.0$  V,  $-3.0$  V,  $-4.0$  V and  $-4.6$  V vs.  $\text{Ag}_{\text{QRE}}$  for 48 h at  $100^\circ\text{C}$  with  $0.4 \text{ mol L}^{-1}$   $\text{Ca}(\text{TFSI})_2$  in EC:PC + 2 wt%  $\text{BF}_3 \cdot \text{DE}$  electrolyte.

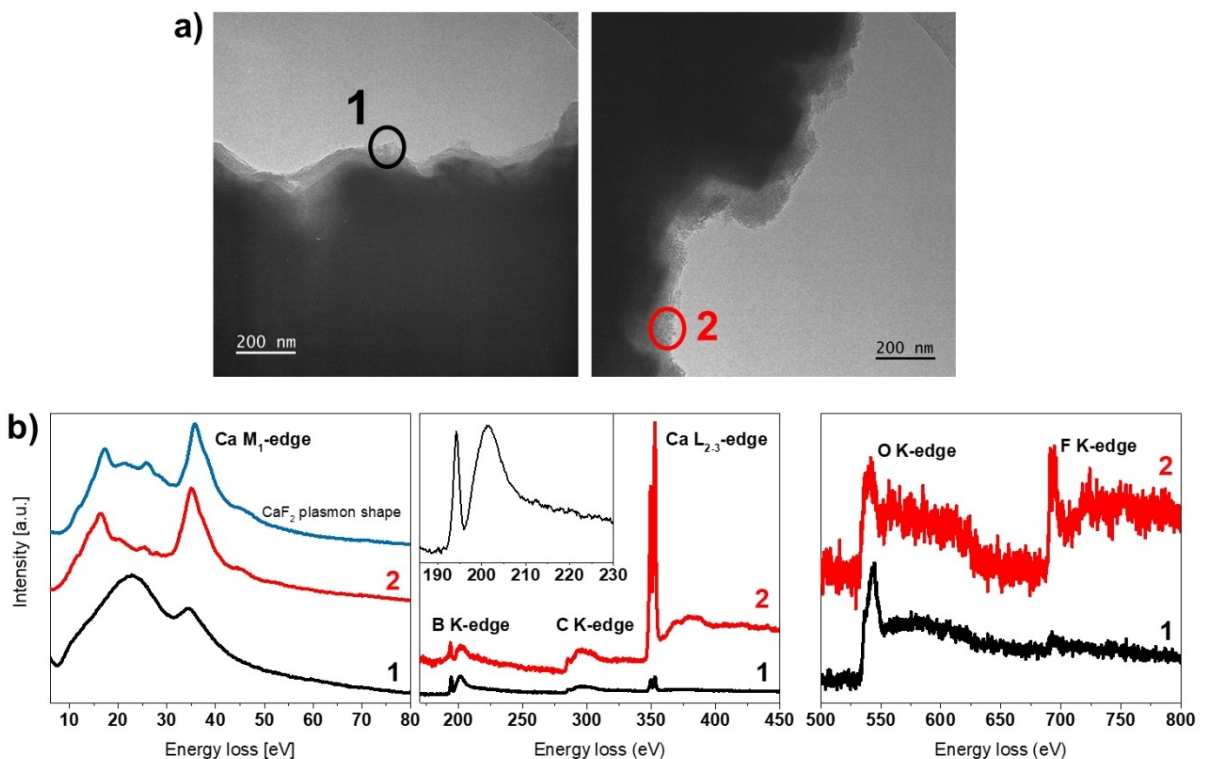


**Figure 4.** a) TEM of passivated nickel particles at a polarization potential of  $-4.0\text{ V}$  vs.  $\text{Ag}_{\text{QRE}}$  during 48 h. b) The associated normalized EELS spectra corresponding to two different areas designated 1 and 2. Spectra normalized by the maximum intensity of signal for plasmon spectra, and the maximum intensity of B K-edge and O K-edge.

### Chemical composition of the SEI

As mentioned earlier, three different microstructures were observed in the passivation layers: an amorphous, conformal layer; some flake-like structure covering the surface; and some crystalline protruding regions. The EELS measurements were performed in two different areas observed by TEM (Figure 4a) and the spectra of B K-edge, C K-edge, Ca L<sub>2,3</sub>-edge, O K-edge, F K-edge, and low-loss region are presented in Figure 4(b). Similar spectra were observed for the amorphous conformal layer and the flake-like structure. The contribution identified in the amorphous region – area noted 1, in black, Figure 4 – confirmed the presence of boron, carbon, oxygen, and calcium. The EELS-spectra obtained were similar to the previous characterization of the SEI obtained with  $\text{Ca}(\text{BF}_4)_2$ -based electrolyte.<sup>[11]</sup> Similarly, the spectrum of B K-edge has an intense initial peak at 194.2 eV followed by a broader peak at 201.2 eV. These two features are common for  $\text{BO}_3$  groups and reveal the tri-coordinated state of the boron species, later confirmed by SR-FTIR.<sup>[15–17]</sup> The EELS analysis in the core-loss region of the second area analyzed, the crystalline area – noted 2 in red, Figure 4 – revealed the presence of Ca and F. The spectra shapes in the low-loss region (energy loss around 50 eV) differ depending on the analyzed area. The plasmon spectrum of the crystalline region – noted 2 in red – has previously been identified as a fingerprint of the  $\text{CaF}_2$  compound, which agreed with the electron diffraction result (Figure S1) and is further confirmed by XPS, as discussed

later.<sup>[11,18]</sup> Boron and oxygen were also detected in the crystalline area (EELS core-loss region), where Ca and F were also identified. In that case, the plasmon fingerprint indicates the presence of  $\text{CaF}_2$ . Two explanations can be formulated for the presence of B and O in the area where the  $\text{CaF}_2$  was detected: i) the  $\text{CaF}_2$  particles are nested in the polymeric matrix formed (containing B and O), which is not obvious as the  $\text{CaF}_2$  compound observed in a previous article was compact and dense;<sup>[11]</sup> ii) the average area of EELS analysis was enlarged in order to avoid degradation of the layer under the beam resulting in averaged contributions from different part of the SEI and the presence of B and O in areas mostly comprising  $\text{CaF}_2$ . As a fact, both components were detected in different ratios as it is shown in Figure S2 some plasmon spectra appear to be a convolution of the  $\text{CaF}_2$  plasmon spectrum and the amorphous-SEI spectrum.

XPS measurements were carried out to further investigate the chemical composition of the passivation layer. The C 1s, F 1s, B 1s and S 2p XPS spectra obtained for layers prepared at the different potentials ( $-2.0$ ,  $-3.0$ ,  $-4.0$  or  $-4.6\text{ V}$  vs.  $\text{Ag}_{\text{QRE}}$ ) are displayed in Figure 5, complemented by the quantitative analysis for each element (Table 1). Ca 2p, N 1s and O 1s spectra are also provided in the Supporting Information, Figure S3.

The signal of nickel (Ni 3p) was not detectable for the samples prepared at  $-4.0\text{ V}$  and  $-4.6\text{ V}$  vs.  $\text{Ag}_{\text{QRE}}$ , suggesting that the nickel disks were fully covered by a layer thicker than 5 nm, which is the probing depth of XPS. However, for

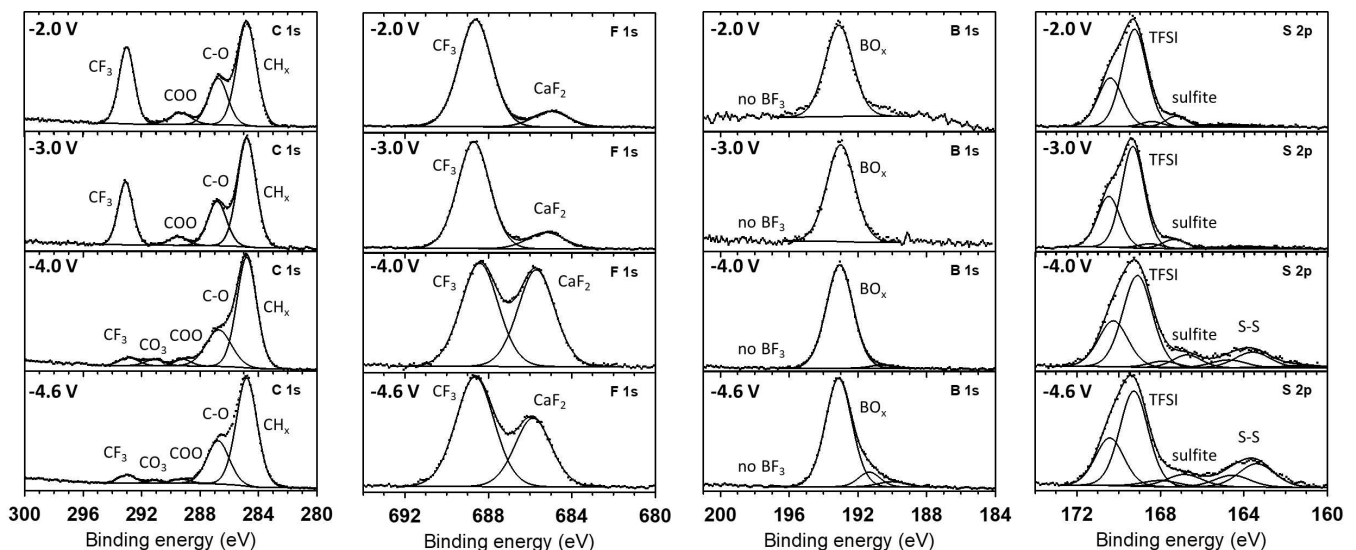


**Figure 5.** C 1s, F 1s, B 1s and S 2p XPS spectra of the surface layer deposited on nickel disks at different potentials (vs. Ag<sub>QRE</sub>). All disks were polarized for 48 h at 100 °C. Spectra are normalized by the most intense contribution.

**Table 1.** Atomic percentage (%) of the components observed in XPS spectra of nickel disks at different potentials of polarization (V vs. Ag<sub>QRE</sub>). Average on three different areas measured on each sample.

Orbital	Potential of polarization						Chemical attribution
	-2.0 V BE [eV]	[%]	-3.0 V BE [eV]	[%]	-4.0 V BE [eV]	[%]	
C 1s	284.8	12.8	284.8	23.5	284.8	19.8	284.8 23.4 C–C, C–H
	286.7	6.0	286.6	8.0	286.4	11.3	286.8 9.9 C–O
	289.2	1.8	289.4	1.7	289.6	1.1	289.1 0.9 COO
	292.9	8.8	293.1	6.0	292.9	1.4	291.4 1.0 CaCO <sub>3</sub>
	348.4	3.6	348.5	4.0	348.4	2.9	348.6 2.2 CF <sub>3</sub> , CaCO <sub>3</sub> , CaO, Ca(TFSI) <sub>2</sub>
	684.8	2.5	685.2	4.8	685.6	3.7	685.9 2.8 CaF <sub>2</sub>
F 1s	688.5	20.9	688.7	14.2	688.5	4.8	688.6 3.6 CF <sub>3</sub>
							189.6 0.9
B 1s					190.6	0.6	191.2 2.3 Borate environment
	193.0	4.6	192.9	6.9	193.0	22.1	193.2 20.7
O 1s	532.7	23.1	532.8	20.2	532.6	25.7	532.7 24.8 Unresolved species
N 1s	399.5	5.1	399.8	3.7	399.8	1.4	400.0 1.1 TFSI
	164.7	0.3	163.9	0.4	163.0	0.4	163.6 0.5 S–S chain
	167.3	0.9	167.3	0.6	166.7	0.3	166.7 0.2 Sulfite
	169.2	9.7	169.3	6.0	169.2	2.1	169.3 1.2 TFSI

polarization potentials of -2.0 V and -3.0 V vs. Ag<sub>QRE</sub>, the nickel signal was detected in some areas, leading to the conclusion that the passivation layers are either thinner or not fully covering the substrate (testimony of the heterogeneity of the surface in the latter case). Nonetheless, the measured quantity of nickel in these cases never exceeded 0.2 at%.

Significant differences were observed in the SEI composition depending on the applied potentials. Carbon content associated to C–C, C–H and oxygenated carbon species was lower in the passivation layer grown at -2.0 V vs. Ag<sub>QRE</sub> ( $\approx$  20 at%) compared to lower potentials (32–34 at%). The TFSI content in the surface layer (i.e., the cumulated at% of XPS signals from N, S, O, C and F corresponding to N, SO<sub>2</sub> and CF<sub>3</sub>) dramatically decreased with the applied potential:  $\approx$  63 at% for -2.0 V,  $\approx$  42 at% for -3.0 V,  $\approx$  14 at% for -4.0 V and  $\approx$  9 at% for -4.6 V vs. Ag<sub>QRE</sub>. At the same time, the S<sub>TFSI</sub>/N ratio

decreased from 1.9 (close to what is expected in TFSI salt) down to 1.1 when the applied potential decreased from -2.0 V to -4.6 V, which reveals a break cleavage of the N–S bond in the anion and evidences TFSI decomposition during SEI formation at low potential. This is further confirmed by the presence of reduced sulfur species in the S 2p spectra for the lowest potentials (Figure 5), corresponding to the formation of elemental sulfur or S–S chains.

Agreeing with EELS, CaF<sub>2</sub> was also evident in the F 1s XPS spectra of the deposited layers (at  $\approx$  685 eV). Its amount fluctuated between 4 and 7 at% in the different samples without any evident trend as a function of the applied potential. CaCO<sub>3</sub> was detected for the samples polarized at -4.0 V and -4.6 V vs. Ag<sub>QRE</sub> (with  $\approx$  1 at% of carbon in CO<sub>3</sub> environment, meaning  $\approx$  5 at% of CaCO<sub>3</sub> compound), whereas it was hardly observed at -2.0 V and -3.0 V vs. Ag<sub>QRE</sub>.

Considering the overall changes of SEI composition, it appears that the amount of carbonates does not have a significant impact.

Finally, applying a lower potential resulted in an increase in the boron content of the surface layer. The layers produced by polarization at  $-2.0\text{ V}$  and  $-3.0\text{ V}$  led to boron contents  $\approx 4$  and  $7\text{ at\%}$ , respectively, while it rose to  $23\text{ at\%}$  when more reductive potentials were applied ( $-4.0\text{ V}$  and  $-4.6\text{ V}$  vs.  $\text{Ag}_{\text{QRE}}$ ). The B 1s spectrum exhibits a main peak at  $193.0\text{ eV}$  corresponding to boron in oxygenated environment, although it is not possible to precisely identify this compound by XPS among the numerous possible species. No evidence of fluorinated environment of B was revealed in the spectra (expected at B 1s binding energies  $>194\text{ eV}$ ), indicating full decomposition of  $\text{BF}_3$  at the surface of the samples, similar to what was observed previously for  $\text{BF}_4$ -derived SEI.<sup>[11]</sup> For the lowest applied potentials ( $-4.6\text{ V}$  especially, and to a lesser extent  $-4.0\text{ V}$  vs.  $\text{Ag}_{\text{QRE}}$ ) two additional B 1s peaks at  $\approx 191$  and  $\approx 190\text{ eV}$  were observed, that might be explained by the appearance of  $\text{CaB}_x\text{O}_y$  species at the surface, ensuing from the decomposition of  $\text{BF}_3$ . The fluoride ligands displaced from the boron additive result in the formation of  $\text{CaF}_2$  as observed before.

The chemical composition of the surface layer found by XPS was confirmed by infrared microspectroscopy analysis of the passivated nickel disks, which provided additional information about the homogeneity of the layers. One representative SR-FTIR spectra of each of the deposited layers at the four different potentials ( $-2.0\text{ V}$ ,  $-3.0\text{ V}$ ,  $-4.0\text{ V}$ , and  $-4.6\text{ V}$  vs.  $\text{Ag}_{\text{QRE}}$ ) are shown in Figure S4 with the spectra of EC:PC mixture and  $\text{Ca}(\text{TFSI})_2$  salt for comparison.

In the IR spectra, three groups of bands will be analyzed separately:

- A number of absorption peaks associated with the TFSI anion, which include the C–F stretching ( $\approx 1240$  and  $1190\text{ cm}^{-1}$ ), the  $\text{SO}_2$  stretching ( $\approx 1317\text{ cm}^{-1}$  and  $\approx 1120\text{ cm}^{-1}$ ), and the S–N–S stretching ( $\approx 1060\text{ cm}^{-1}$ ).<sup>[19]</sup>
- A broad band observed between  $1280$  and  $1550\text{ cm}^{-1}$  but does not allow a precise attribution of the individual peaks in this region. However, knowing the compounds in presence, it is expected to include a convolution of some vibrational modes of  $\text{SO}_2$  ( $1310\text{ cm}^{-1}$ ), the  $\text{CH}_2$  wagging ( $1340\text{ cm}^{-1}$ ), and the B–O stretching (around  $1480\text{ cm}^{-1}$ ), all of them arising from decomposition products of the components of the electrolyte.
- The presence of one or several bands between  $1600$ – $1800\text{ cm}^{-1}$ , which are linked with the presence of C=O functional groups in different environments.<sup>[20]</sup> From the original  $1770$  and  $1787\text{ cm}^{-1}$  positions in the neat solvent, a low-frequency shift in the band evidences the reductive decomposition of the solvent, producing new chemical compounds containing C=O, such as oxalate.<sup>[21,22]</sup>

The different vibration components change in intensity ratio depending on the potential used for deposition, evidencing changes in the chemical composition of the different surface layers. Additionally, the relative intensity of the different components also changes at different points across the surface of each sample, as will be later described.

SR-FTIR microspectroscopy can resolve the different contributions from different regions of the passivation layer with a spatial resolution of  $10\times 10\text{ }\mu\text{m}$  and clearly evidence differences in surface homogeneity. Figure 6 shows the IR chemical maps

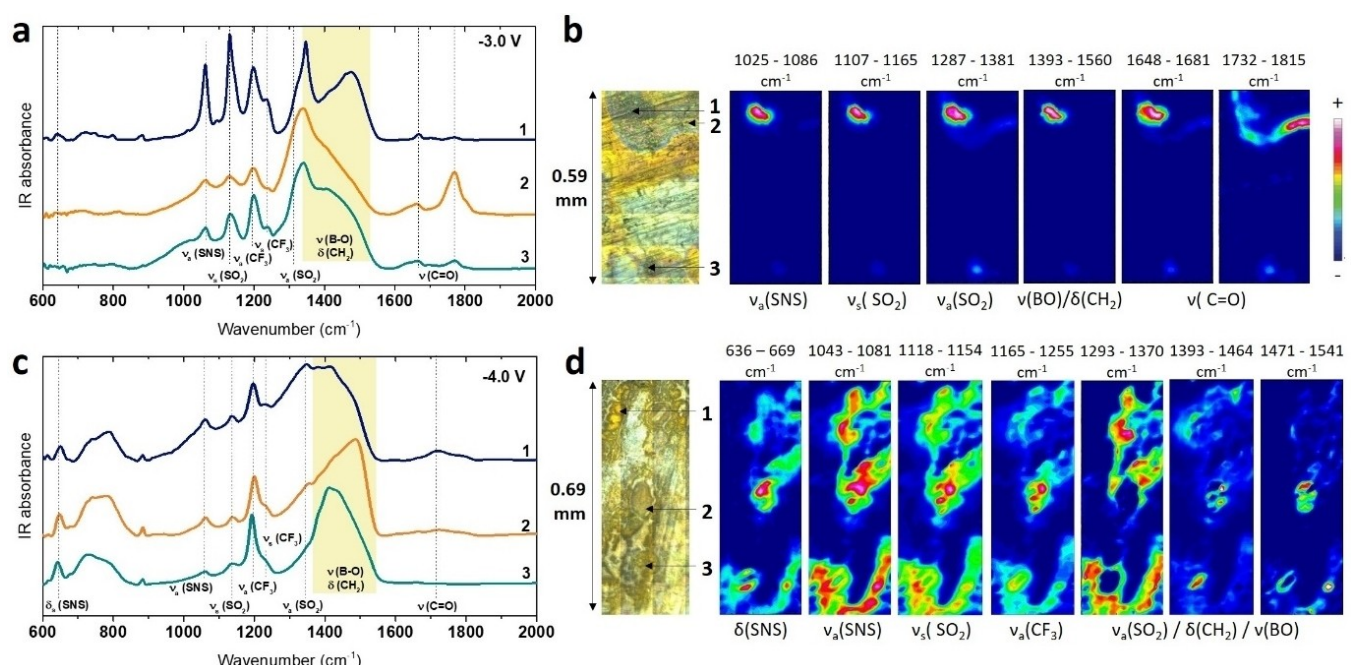


**Figure 6.** IR analysis of the SEI layers for the samples polarized during 48 h at a, b)  $-3.0\text{ V}$  and c, d)  $-4.0\text{ V}$  vs.  $\text{Ag}_{\text{QRE}}$ . a, c) FTIR-microspectroscopy spectra of the regions 1, 2, 3 marked on panels (b) and (d), dash lines are guides for the eye. b, d) Associated chemical images of the surface of the deposit for particular bands. The color scale corresponds to the intensity of the respective FTIR peak.

of two of the prepared surface layers, particularly the ones prepared at potentials higher or lower than the onset for calcium plating potential ( $-3.0\text{ V}$  and  $-4.0\text{ V}$  vs.  $\text{Ag}_{\text{QRE}}$ , respectively), together with the measured IR spectra of some specific points. The IR chemical maps obtained for the layers deposited at  $-2.0$  and  $-4.6\text{ V}$  vs.  $\text{Ag}_{\text{QRE}}$  are provided in the supplementary information, Figure S5.

On the surface layer produced at  $-3.0\text{ V}$  vs.  $\text{Ag}_{\text{QRE}}$  (Figure 6a and b), the point marked as 1 appears to be part of a TFSI-rich area, as all the bands associated with the anion vibration modes [group of bands (i) described above] are well distinct and with the highest intensity compared to the other bands of the spectrum. Point 2, on the other hand, has a higher population of carbonyl-containing products, in which the carbonyl stretching band is near one of the neat solvents ( $1770\text{ cm}^{-1}$ ), while point 3 evidences some carbonyl bond with lower vibration frequency ( $1670\text{ cm}^{-1}$ ) attributed to solvent degradation products.

In the case of the sample polarized at  $-4.0\text{ V}$  vs.  $\text{Ag}_{\text{QRE}}$ , Figure 6(c and d), TFSI bands are still observable but with lower intensity in regards to the broad band attributed notably to  $\text{CH}_2$  and  $\text{BO}$  moieties. Interestingly, this broad peak has different shapes depending on the position meaning there are differences in terms of local composition at the surface of the sample. The full spectra comparison of various points on the surface of the sample, Figure S6, revealed the presence of  $\text{CH}_2$  and  $\text{CH}_3$  stretching bands around  $2870$ ,  $2927$  and  $2960\text{ cm}^{-1}$  only when the band around  $1340\text{ cm}^{-1}$  is also present, as it is on the position 1. Based on this, we attribute the band at  $1340\text{ cm}^{-1}$  to the  $\text{CH}_2$  bending (wagging mode). As was the case of the layer produced at  $-3.0\text{ V}$  vs.  $\text{Ag}_{\text{QRE}}$ , the IR chemical maps (Figure 6b) reveal the heterogeneities in the chemical distribution of species, particularly visible in the three last maps, between  $1290$ – $1370$ ,  $1390$ – $1460$ , and  $1470$ – $1540\text{ cm}^{-1}$ , respectively. It is also worth noting that larger “blue areas” (low FTIR peak intensity) were observed for samples prepared at  $-2.0$  and  $-3.0\text{ V}$  vs.  $\text{Ag}_{\text{QRE}}$  confirming the thinner nature of the passivation layers formed.

The surface layer produced at  $-4.6\text{ V}$  vs.  $\text{Ag}_{\text{QRE}}$ , being the thickest, allowed for the measurement of high-quality far-IR spectra (Figure S7). An interesting feature around  $617\text{ cm}^{-1}$  is possibly attributed to the in-plane bending of the trigonal or tetragonal boron compound, as compared to the spectra of the reference compounds shown in Figure S8. As previously reported, the in-plane bending of the fully symmetrical  $[\text{BO}_3]^{3-}$  anion, presents for example in  $\text{Ca}_3\text{B}_2\text{O}_6$ , lies between  $615$ – $625\text{ cm}^{-1}$ , similarly to the dimeric  $[\text{B}_2\text{O}_5]^{4-}$  anion (from  $\text{Ca}_2\text{B}_2\text{O}_5$ ), confirming the trigonal coordination of the boron observed by EELS analyses. In the case of the polymeric  $(\text{BO}_2^-)_n$  anion, this vibration mode gets high-frequency shifted to  $633\text{ cm}^{-1}$  due to the more rigid backbone of  $-\text{B}-\text{O}-\text{B}-\text{O}-$  chains and the lower symmetry.<sup>[23]</sup> Thus, a band at  $617\text{ cm}^{-1}$  suggests that the boron centers are not participating in infinite chains of trigonal moieties, but instead are present as isolated  $\text{BO}_3$  groups, possibly in a carbon polymeric chain (Figure S9).

ToF-SIMS analysis further supports the idea that the surface layer is composed of  $\text{BO}_3$  moieties cross-linked in an organic

polymeric matrix (Figure S10). Across the surface, the peaks related to boron species (particularly  $\text{B}^+$   $m/z=11$ ) are always present together with fragments related to organic species  $m/z=27$  ( $\text{C}_2\text{H}_3^+$ ) and  $m/z=83$  ( $\text{C}_5\text{H}_9\text{O}^+$ ), and even higher molecular weight polymer fragments  $m/z=209$ ,  $185$  and  $161$ .

## Mechanism of the SEI formation

To shed light on the mechanism of formation of the  $\text{BF}_3$ -derived passivation layer, it is first crucial to determine the species initially present in the solution. Upon addition of  $\text{BF}_3\cdot\text{DE}$  into the  $\text{Ca}(\text{TFSI})_2$  in EC:PC electrolyte, the carbonate solvents may displace the diethyl ether and bind directly to the  $\text{BF}_3$ . To corroborate this direct interaction, we measured the IR spectra of the neat electrolyte and the electrolyte after the addition of the  $\text{BF}_3\cdot\text{DE}$  adduct (Figure S11). The presence of a new band centered at  $1678\text{ cm}^{-1}$  confirms the formation of  $\text{BF}_3\cdot\text{EC}$  and/or  $\text{BF}_3\cdot\text{PC}$  adducts in solution, as it can be assigned to the carbonyl stretching vibration of these carbonates when complexed by  $\text{BF}_3$  (Figure S12).<sup>[24]</sup>

## DFT calculation of the reduction process of the $\text{BF}_3\text{ EC}$ complex

Possible decomposition process was further investigated by DFT. The reduction of free EC molecules requires very low potential, below  $-1\text{ V}$  vs. Ca, as shown in Figure S14, and thus some shift of electron density is needed to ease the electron transfer. By coordination with a strong Lewis acid like  $\text{BF}_3$ , some electron density is withdrawn from the EC, decreasing the charge at the boron atom from  $+1.45|\text{e}|$  to  $+1.34|\text{e}|$ . As a result, the first and second reductions of  $\text{BF}_3\cdot\text{EC}$  complex occur at much higher potentials than the observed for pure EC. The obtained reduction potentials are  $0.99$  and  $0.23\text{ V}$  vs. Ca, respectively, both being above the potential of metallic calcium, Figure 7. The first reduction step leads to a structure quite stable, which could undergo decomposition through  $\beta$  cleavage, i.e., breaking of the bond between the oxygen at  $\beta$  position in the ring and the carbon in  $\gamma$ , although this ring-opening has a high energetic barrier of around  $73\text{ kJ mol}^{-1}$ . Hence, instead of an immediate decomposition, the second reduction is most probable, followed by competition between the  $\alpha$  and the  $\beta$  cleavages of the ring (see Figure 7). The product obtained by  $\beta$  cleavage is more stable, leading eventually to inorganic  $\text{CO}_3^{2-}$  and ethylene, but being restricted by the higher energetic barrier of  $29\text{ kJ mol}^{-1}$ . On the other hand, the breaking of the  $\alpha$  bond requires only  $21\text{ kJ mol}^{-1}$  and leads to a  $\text{BF}_3$  adduct that can undergo further polymerization reactions which will be further explored (Figures 7 and S15).

Given the energetic preference for decomposition of the doubly reduced EC ring by  $\alpha$  cleavage, we followed more closely the reaction path occurring after the breaking of this bond (Figure S15b), which is expected to have a great impact on the formation of the SEI layer. Two main alternatives are examined: i) the nucleophilic  $-\text{O}^-$  group can attack the carbonyl carbon of an EC molecule nearby promoting further

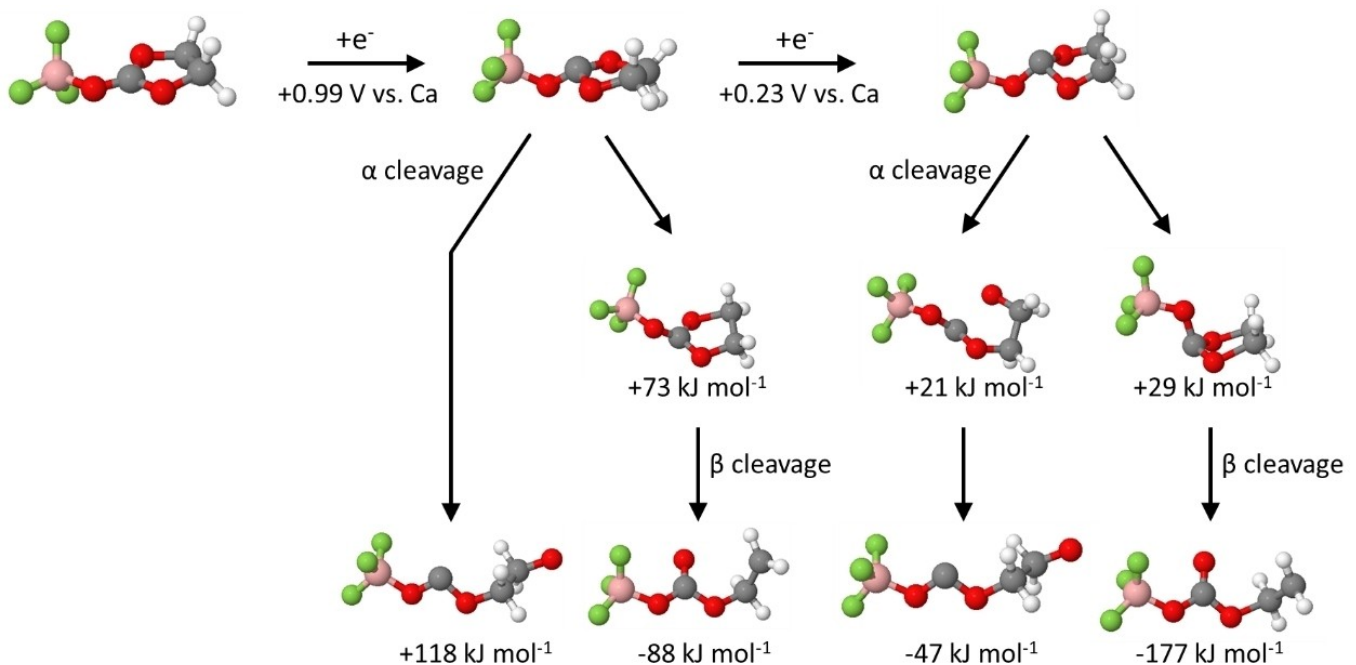


**Figure 7.** Reduction process of  $\text{BF}_3\text{-EC}$  complex and possible initiation steps.  $\alpha$  and  $\beta$  cleavages are analyzed as possible decomposition steps of the singly and doubly reduced forms.

polymerization and SEI growth, and ii) the species can spontaneously decompose releasing  $\text{CO(g)}$ , both alternatives are depicted in Figure 8a and the energetic barriers for each step in the reaction are given in Figure S15(b). From the energy point of view, the former mechanism is preferred. This attack on another EC molecule promotes its ring-opening and further polymerization, as depicted in Figure S15(b), in which boron centers are included as crosslinking points.

To further explore the possibility of boron centers as crosslinking points, we studied the possibilities of exchanging the  $\text{F}^-$  ligands by other species in solution, e.g., EC solvent. The performed potential energy scan of the  $\text{B}-\text{O}$  and  $\text{B}-\text{F}$  bond lengths showed that such reaction would need to go through

mononuclear nucleophilic substitution ( $\text{S}_{\text{N}}1$ ), with fluoride anion leaving the boron center before the attack of EC molecule, Figure 9(a). This pathway results, however, in a significant energy barrier (ca.  $150 \text{ kJ mol}^{-1}$ ) which is a direct result of the strong  $\text{B}-\text{F}$  bond in these complexes, limiting the direct fluoride ligand exchange.<sup>[25]</sup> Such high energy penalty discards the reaction via a  $\text{S}_{\text{N}}1$  mechanism and led us to consider the role of  $\text{Ca}^{2+}$  cations.

The situation is drastically modified by accounting for the effect of  $\text{Ca}^{2+}$  in the vicinity of the boron centers. When  $\text{Ca}^{2+}$  is close to the leaving fluoride atom, EC molecule is able to attack the boron center and form five coordinated transition states according to  $\text{S}_{\text{N}}2$  reaction mechanism, corresponding to an

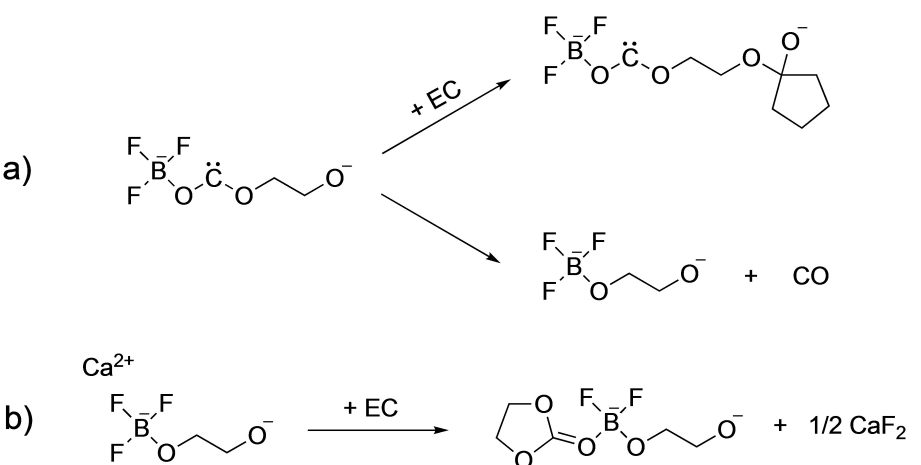


**Figure 8.** Depiction of the most probable reactions after reductive decomposition of  $\text{BF}_3\text{-EC}$  complex. a) Elongation of the polymeric sidechain, and b) fluoride ligand substitution in the boron centers leading to polymer crosslinking.

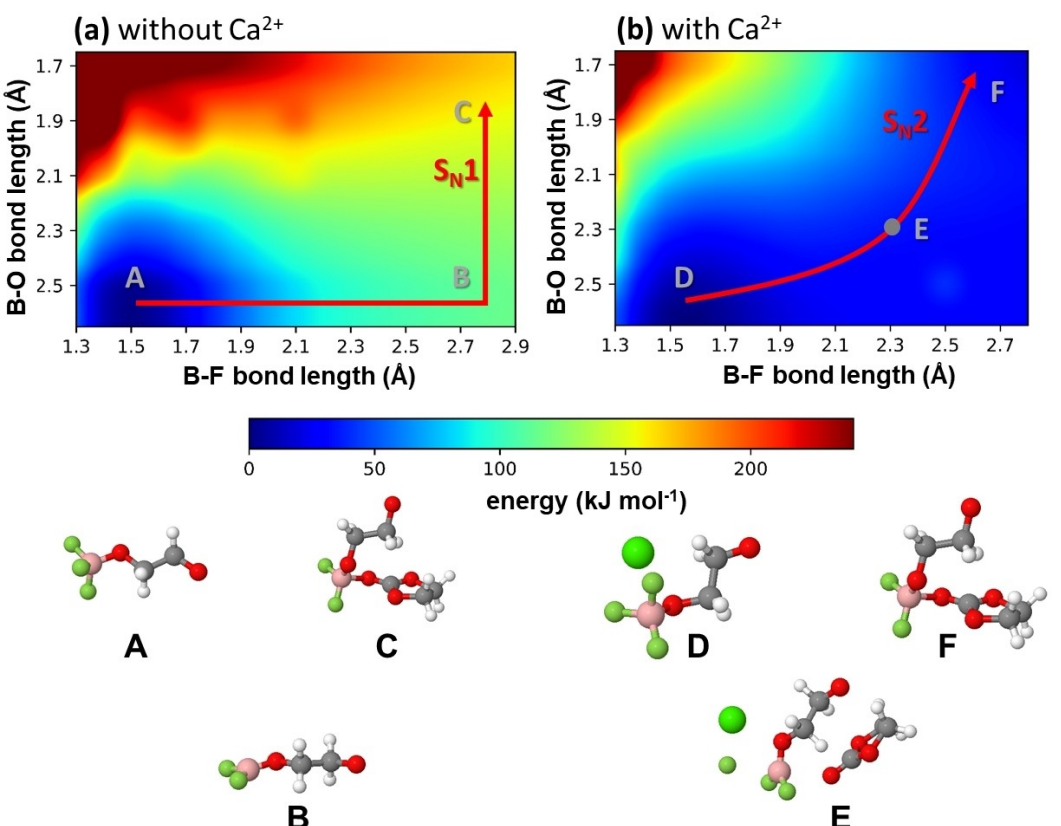


**Figure 9.** Potential energy surfaces during ligand exchange of a fluoride anion to an EC molecule at the boron center, as function of B–O and B–F bond lengths. Figure present situation for a)  $\text{BF}_3\text{-OC}_2\text{H}_2\text{O} + \text{EC}$  and b)  $\text{CaBF}_3\text{-OC}_2\text{H}_2\text{O} + \text{EC}$ . Different points across the reaction pathway are marked (A–E), and their molecular structures are presented.

energetic barrier of 56 kJ mol<sup>-1</sup>, Figure 9(b). Then, the fluoride ligand can leave the boron center forming  $\text{CaF}^+$ , a similar mechanism proposed before for ligand exchange of  $\text{BF}_3$  complexes, in which fluoride ligand exchange is favored by the collaborative effect of Lewis acid species that can accept the leaving  $\text{F}^-$  ligand.<sup>[26]</sup> The energy increase for this reaction is significantly lower than in the previous case (43 kJ mol<sup>-1</sup>) which is compensated by the precipitation of solid  $\text{CaF}_2$ . Indeed, the formation of crystalline  $\text{CaF}_2$  and its precipitation is a highly exothermic process (the heat of sublimation for  $\text{CaF}_2$  is 419 kJ mol<sup>-1</sup>) leading to an overall negative enthalpy of reaction and indicating a thermodynamic preference for fluoride ligand exchange whenever  $\text{Ca}^{2+}$  ions are present in the solution.<sup>[27]</sup> This ligand exchange can proceed further until all the fluoride ligands are substituted by O–R groups producing boron-crosslinked polymers.

This can be linked to the electrochemical results obtained Figure 1, where applying lower potentials ( $-4.0$  and  $-4.6$  V vs.  $\text{Ag}_{\text{QRE}}$ ) favor calcium plating/stripping. In such cases, the presence of boron center in crosslinked polymers seems favored by a polarization at lower potential than the reduction potential of calcium. XPS results confirm a higher borate content for the lowest potential of polarization, which is more favorable to calcium diffusion.

#### Other $\text{BF}_3$ adducts as additives

As a way to confirm that the  $\text{BF}_3\text{-EC}$  is responsible for the beneficial aspects of this electrolyte mixture, the  $\text{BF}_3\text{-EC}$  adduct was synthesized and included as an additive in a 0.4 mol L<sup>-1</sup>  $\text{Ca}(\text{TFSI})_2$  in EC:PC electrolyte. Infrared characterization and Raman Spectroscopy of the synthesized  $\text{BF}_3$  complex are provided Figures S12 and S13. CVs performed using the electrolyte formulation including this additive exhibit very similar redox features when compared with CVs obtained with  $\text{BF}_3\text{-DE}$ -based electrolytes, with evidence of redox processes occurring centered around  $-2.9$  V vs.  $\text{Ag}_{\text{QRE}}$  attributed to calcium plating and stripping, Figure S16(a).

The same concept can be extended to other  $\text{BF}_3$  complexes. Three other complexes were synthesized:  $\text{BF}_3\text{-DMC}$ ,  $\text{BF}_3\text{-DEC}$ ,  $\text{BF}_3\text{-}\gamma\text{BL}$  (where DMC: dimethyl carbonate, DEC: diethyl carbonate, and  $\gamma$ BL:  $\gamma$ -butyrolactone), infrared and Raman characterizations are provided, Figures S12 and S13, and their crystal structure was determined by single-crystal X-ray diffraction (Figures S17, S18, and Tables S1–S5). These boron-based additives were added to the electrolyte and electrochemical results were compared (Figure S16b). Calcium reduction and oxidation were observed with each additive, which suggests that a beneficial SEI layer for calcium plating/stripping is being formed in all cases and that the decomposition mechanism studied above applies for different  $\text{BF}_3$  complexes.

While the nature of the polymeric chains might differ depending on the solvent being initially complexed with  $\text{BF}_3$ , the mechanisms behind the growth of boron cross-linked polymers, involving fluoride ligand substitution, and favored by the presence of a Lewis acid, are expected to be similar. In fact, while Lewis acid additives [such as TPFPB: tris(pentafluorophenyl)borane] have been previously studied as anion-trapping agents in lithium-ion electrolytes, their influence on the SEI formation mechanisms is seldom presented but can have a significant effect in the operation of a battery.<sup>[28]</sup>

## Conclusion

The understanding and further engineering of the interfaces between the electrodes and the electrolyte in any battery technology are of paramount importance. Here, we provided a comprehensive study of the SEI being formed during calcium deposition from an electrolyte mixture containing different  $\text{BF}_3$  adducts, connecting experimental evidences of its composition, morphology, and homogeneity with a mechanistic study proposed by DFT results.

We demonstrated that the SEI formed when  $\text{BF}_3\cdot\text{DE}$  is included as electrolyte additive is rich in borate species present as  $\text{BO}_3$  groups in a cross-linked polymeric matrix, although with some heterogeneities across the surface. Other species that were detected in the SEI are  $\text{CaF}_2$  and TFSI decomposition products. The potential at which the passivation layer is being formed appeared as a crucial parameter, and polarizing the electrode below the  $\text{Ca}^{2+}/\text{Ca}$  standard potential was required to increase the formation of borates, decrease the presence of TFSI-based components and favor calcium plating and stripping. By contrast, passivation layers formed at higher potential do not allow direct plating/stripping of calcium unless continuous cycling at lower potential is performed.

The coordination of the carbonate solvent by  $\text{BF}_3$  was demonstrated and found to favor the reductive decomposition of the solvent, with the formation of boron cross-linked polymer chains, explaining the high boron content observed in the SEI. A crucial step in the SEI formation is the substitution of the fluoride ligands of the boron additive, which was found to be promoted by the presence of  $\text{Ca}^{2+}$  via the precipitation of the highly stable  $\text{CaF}_2$ . Thus, the increase of cation concentration in the electrode vicinity upon polarization at or below the Ca plating onset potential was identified as a crucial parameter favoring the growth of borate cross-linked polymers.

The findings of this study suggest that a boron-containing polymer in the surface layer is key to allow  $\text{Ca}^{2+}$  migration and to permit metal plating and stripping, such layer thus acting as a Ca-based SEI. Different  $\text{BF}_3$  adducts involving various solvents (EC, DMC, DEC and  $\gamma$ BL) were prepared and studied as additives and appear to promote Ca plating and thus the formation of similar boron cross-linked polymers. These results pave the way to very rich chemistry for SEI derived from boron-based Lewis acids binding directly to different solvents and open the possibility to the development of artificial SEI for Ca metal anode.

## Experimental Section

**Electrolyte preparation:** The electrolyte was composed of calcium bis(trifluoromethanesulfonyl)imide,  $\text{Ca}(\text{TFSI})_2$ , (99.5% purity, Solvionic) at a concentration of  $0.4 \text{ mol L}^{-1}$  dissolved in a 50/50 wt% mixture of ethylene carbonate (EC, from Sigma-Aldrich, anhydrous, 99.0%) and propylene carbonate (PC, from Sigma-Aldrich, anhydrous, 99.7%). The salt was dried under vacuum for 12 h at  $100^\circ\text{C}$ . The solvent mixture was dried over molecular sieves (3 Å from Alfa Aesar) for a minimum of 2 days. Different  $\text{BF}_3$ -complexes were studied as additives in the liquid electrolyte. The boron trifluoride diethyl ether ( $\text{BF}_3\cdot\text{DE}$ ) was purchased from Sigma Aldrich and used without further purification. Other  $\text{BF}_3$ -complexes with other solvents were prepared by the method detailed later down. In all cases a 2 wt.% of the different additives were introduced in the electrolyte for testing.  $\text{BF}_3$  and  $\text{BF}_3$ -complexes are very toxic and must be handled with special care.

**$\text{BF}_3$ -complexes preparation:** The  $\text{BF}_3$  adducts were prepared following a method similar to that reported before by Eisele et al.<sup>[24]</sup> The handling of  $\text{F}_2$  and  $\text{BF}_3$  was performed in a metal vacuum line (nickel, copper) equipped with Monel Helicoid pressure gauges, PTFE (polytetrafluoroethylene) valves, a soda lime scrubber, liquid-nitrogen-cooled traps, and a two-stage rotary vacuum pump. The reaction vessels consisted of an FEP tube (8.0 mm outer diameter, 5.7 mm inner diameter, 21 cm long;  $V=5.9 \text{ mL}$ ) equipped with a PTFE valve. The reaction vessels were passivated with  $\text{F}_2$  prior to use.

Approximately 170 mg (~1.9 mmol) of ethylene carbonate (EC), dimethyl carbonate (DMC), diethyl carbonate (DEC) or  $\gamma$ -butyrolactone ( $\gamma$ BL) were loaded in the reaction vessel inside a nitrogen-filled glovebox. The reaction vessel was then connected to the vacuum line, cooled down in a liquid-nitrogen bath and evacuated to remove the inert gas inside. Stepwise additions of ~0.4 mmol of  $\text{BF}_3$  were condensed into the FEP reaction vessel using a liquid-nitrogen bath. The reaction vessel was warmed up slowly after each addition to allow complete reaction and to follow its evolution. In all cases, the initially clear solution turns into a cloudy suspension after the initial addition steps. The fraction of the solid product in the reactor increases as the addition continues. A complete consumption of the  $\text{BF}_3$  after each addition was evidenced by a negligible vapor pressure (<5 Torr) inside the reactor. After the equivalent point was reached, the reactor was left overnight with a slight overpressure of  $\text{BF}_3$  (~50 Torr, 0.02 mmol). The vessel was then evacuated, transferred to a glovebox and the solid product was slightly ground with a metallic rod. A final addition of ~0.4 mmol of  $\text{BF}_3$  was done and the reaction was left for 24 h to ensure completeness. The vessels were then fully evacuated at  $-20^\circ\text{C}$  to avoid the decomposition of the solid complex and transferred to the glovebox. The white solid was recovered in all cases and stored under argon atmosphere until use.

**Electrochemical measurements:** The 3-electrode Swagelok cells were assembled with a working electrode (WE) composed of a nickel disk (Goodfellow, Ø10 mm) or nickel powder (99.9%, APS 3–7 micron, from Alfa Aesar), a calcium disk (99.5%, Alfa Aesar) as a counter electrode (CE) and a silver wire (Sigma Aldrich) as quasi-reference electrode.<sup>[29]</sup> A cellulose separator was used, in addition to a Whatman glass microfiber to prevent adhesion with the Ni disk and help the recovery of the substrate for further analyses. The electrolyte was constituted of a salt diluted in EC:PC mixture with a 1:1 weight ratio. A volume of 0.4 mL of electrolyte was added to the cells. The working electrodes were polarized at various potentials ( $-2.0 \text{ V}$ ,  $-3.0 \text{ V}$ ,  $-4.0 \text{ V}$ , and  $-4.6 \text{ V}$  vs.  $\text{Ag}^{\text{ORE}}$ ), the potential was reached by linear sweep voltammetry at  $0.1 \text{ mV s}^{-1}$  and then maintained for 48 h at  $100^\circ\text{C}$ . The calcium (in

the cases of a calcium deposit) was then stripped from the surface of the nickel with linear sweep voltammetry to the initial open-circuit voltage, at 0.1 mV s<sup>-1</sup>.

**Transmission electron microscopy and electron energy loss spectroscopy:** The microstructural and chemical characterizations of the electrodes were performed using a TECNAI F20-S-Twin operating at 200 kV and equipped with an electron energy loss spectrometer (EELS) Gif Tridiem in the post column. The acquisitions of the energy-loss near-edge structures (ELNES) were performed in diffraction or scanning transmission electron microscopy (STEM) modes. The reported measurements were performed using an energy resolution of 1–1.2 eV and determined by measuring the full width at half the maximum of the zero-loss peak. The following conditions were used to acquire the EELS spectra: a dispersion of 0.2 eV ch<sup>-1</sup>, a convergence angle of 5.8 mrad, and a collection angle of 21.7 mrad. For the core loss of the B, Ca, O, and F K-edges: the background was subtracted considering a power-law function.<sup>[30]</sup> The multiple scatterings were removed using the Fourier-ratio method and energy correction was performed with respect to the zero-loss peak calibrated to 0 eV. To limit the irradiation effect and give reliable results, the TEM/EELS investigations were done in low-dose mode and using specific tunings determined after a prior irradiation study on the samples. The tuning and the analyses were also performed on different areas to avoid unnecessary irradiation of the area of interest. For the characterization with TEM, 15 mg of nickel powder (99.9%, APS 3–7 micron, from Alfa Aesar) was used as the working electrode. After the electrochemical step, the powder was rinsed several times with dimethyl carbonate (DMC). The particles were dispersed in DMC to be placed over a gold TEM olefin carbon grid. The transfer of the grids between the argon glove box and the TEM was performed without air exposure according to the previously reported procedure.<sup>[31]</sup>

**X-ray photoelectron spectroscopy:** The equipment used was a Thermo Scientific ESCALAB 250 spectrometer, using a focused monochromatized Al K $\alpha$  radiation ( $h\nu=1486.6$  eV). The pressure was maintained around 10<sup>-8</sup> mbar and charge neutralization was applied. The analyzed area of the samples was an ellipse with a dimension of 450  $\mu\text{m} \times 900$   $\mu\text{m}$ . The binding energy scale was calibrated from the carbon present in the sample using the C 1s peak at 284.8 eV. The XPS transfer chamber was directly connected to an argon glovebox to prevent the samples' surfaces from any contact with air and moisture during the transfer. Samples were thoroughly rinsed with dimethyl carbonate solvent to remove the electrolyte before analysis.

**Fourier transform infrared microspectroscopy:** Samples realized in the same conditions than XPS were analyzed but couldn't be prevent from air contact. A Vertex 70 spectrometer was coupled to a Hyperion 3000 microscope (Bruker, Germany) to perform Synchrotron-based FTIR microspectroscopy measurements at the MIRAS beamline of the ALBA synchrotron light source (Barcelona, Spain). The microscope is equipped with a liquid N<sub>2</sub> cooled HgCdTe 50  $\mu\text{m}$  MCT detector and uses a 36 $\times$  Schwarzschild objective (NA = 0.52). The spectra were obtained in trans-reflection mode, using a masking aperture size of 10  $\mu\text{m} \times 10$   $\mu\text{m}$ . Raster scanning maps were collected in the mid-IR range (4000–700 cm<sup>-1</sup>) with a step size of 10 $\times$ 10  $\mu\text{m}$  at a spectral resolution of 4 cm<sup>-1</sup> with 64 co-added scans per spectrum.

Measurements in the Far-IR range (600–350 cm<sup>-1</sup>) were performed under the same FTIR instrument mentioned above by using a bolometer detector and 15 $\times$  Schwarzschild objective (NA = 0.40). Due to the special resolution, which is diffraction limited and is about half of the wavelength, the spectra were obtained using a masking aperture size of 50  $\mu\text{m} \times 50$   $\mu\text{m}$  in trans-reflection mode.

**Time-of-flight secondary ion mass spectrometry:** ToF-SIMS analysis were performed using a TRIFT V Nano ToF II Tandem MS (Physical Electronics, Chanhassen (MN), US) equipped with a 30 kV Bi<sub>n</sub><sup>+</sup>-LMIG primary ion gun. The electrode samples were fixed with a metallic mask on the sample holder and transferred from the gloves box to the spectrometer using a transfer vessel to avoid any air exposure. For surface analysis, all mass spectra were acquired using the same experimental conditions which allow performing semi-quantitative analysis (comparing the ratio of peaks intensities): the LMIG gun was tuned to deliver Bi<sup>3+</sup> primary ions with a DC current of 12 nA over a 50 $\times$ 50  $\mu\text{m}^2$  raster size, the mass range was fixed between 0 and 800  $\mu\text{m}$  and the number of frames was set to 30 (dose: 3.3 $\times$ 10<sup>12</sup> ions cm<sup>-2</sup>) for both positive and negative polarities.

Data processing was performed using ToF-DR software provided by Physical Electronics. All positive polarity mass spectra were calibrated using B<sup>+</sup> ( $m/z=11$ ), Na<sup>+</sup> ( $m/z=23$ ), and CH<sup>+</sup> ( $m/z=13$ ) peaks and all negative polarity spectra were calibrated using CH<sup>-</sup> ( $m/z=13$ ), F<sup>-</sup> ( $m/z=19$ ), and S<sup>-</sup> ( $m/z=32$ ) peaks.

**Raman spectroscopy:** the measurements were conducted on a Horiba Jobin-Yvon LabRam HR confocal Raman system. Raman spectra were recorded at room temperature over the spectral range of 50–4000 cm<sup>-1</sup> using the 532 nm emission line of a diode-pumped solid-state laser (Torus, Laser Quantum) with a power output of  $\approx 12$  mW on the sample. The samples, liquids and powdered crystalline solids, were transferred into quartz capillaries (which were heat/vacuum-dried and pre-treated with F<sub>2</sub>) in a glovebox and closed with inert halocarbon grease or flame-sealed.

**Computational methods:** DFT calculations were performed using M06-2X and 6-311++G(d,p) basis set as implemented in Gaussian 16. To better mimic the electrolyte surrounding the conductor-like polarizable continuum model (C-PCM) using parameters for THF was applied for all species. All the formation energies of different species were calculated based on the Gibbs free energies. The scan of the bonds was performed using the tool implemented in Gaussian 16 software, with optimization done after each change of the bond distance by 0.1 Å. For the electrode reactions, the reduction potentials were calculated from a thermodynamic cycle and converted to Ca<sup>2+</sup>/Ca scale by -1.56 V, while the charge distributions were obtained from Natural Population Analysis (NPA).

**Single-crystal X-ray diffraction:** Crystal structure determinations were carried out on a Rigaku OD XtaLAB Synergy-S single-crystal X-ray diffractometer equipped with microfocus Ag and Cu sources and an Eiger2 R CdTe 1 M hybrid pixel detector. *CrysAlisPro* software<sup>[32]</sup> was employed for data collection and processing. Structures were solved by *olex2.solve*<sup>[33]</sup> or *Superflip*,<sup>[34,35]</sup> and refined with *SHELXL*<sup>[36]</sup> implemented within the *Olex2* (v. 1.5) program. *Diamond*<sup>[37]</sup> program was used for crystal structure visualization. Hydrogen atoms were freely refined including an isotropic thermal parameter.<sup>[38]</sup> Crystal selection and mounting was carried out at low temperature (about -50 to -60 °C) under protective cold nitrogen stream employing a previously described low-temperature crystal mounting procedure.<sup>[39]</sup>

The crystal structures of BF<sub>3</sub> $\cdot$ OC(CH<sub>3</sub>)<sub>2</sub> and BF<sub>3</sub> $\cdot$ OC(OCH<sub>2</sub>)<sub>2</sub> measured at 150 K are in good agreement with previously determined structures<sup>[24]</sup> at 100 K:

BF<sub>3</sub> $\cdot$ OC(OCH<sub>2</sub>)<sub>2</sub> [*Pbca*,  $a=9.7135(2)$  Å,  $b=9.8393(2)$  Å,  $c=11.3749(3)$  Å,  $V=1087.15(4)$  Å<sup>3</sup>], CCDC number: 1972336.<sup>[24]</sup>

BF<sub>3</sub> $\cdot$ OC(CH<sub>3</sub>)<sub>2</sub>, [*P2<sub>1</sub>/n*,  $a=6.8416(2)$  Å,  $b=14.4962(4)$  Å,  $c=6.9580(2)$  Å,  $\beta=115.8250(10)$ °,  $V=621.16(3)$  Å<sup>3</sup>], CCDC number: 1972338..<sup>[24]</sup>

Deposition Number(s) 2176723 [for  $\text{BF}_3\cdot\text{OC}(\text{OCH}_2)_2$ ], 2176724 [for  $\text{BF}_3\cdot\text{OC}(\text{OCH}_3)_2$ ], 2176725 [for  $\text{BF}_3\cdot\text{OC}(\text{OCH}_2\text{CH}_3)_2$ ], 2176726 [for  $\text{BF}_3\cdot\text{OC}(\text{CH}_2)_3\text{O}$ ] contain(s) the supplementary crystallographic data for this paper. These data are provided free of charge by the joint Cambridge Crystallographic Data Centre and Fachinformationszentrum Karlsruhe Access Structures service.

## Supporting Information

Supporting Information is available from the Wiley Online Library or from the author.

## Acknowledgements

Funding from the European Union's Horizon 2020 research and innovation program H2020 are acknowledged: European Research Council (ERC-2016-STG, CAMBAT, grant agreement no. 715087 and ERC-2020-STG, HiPeR-F, grant agreement no. 950625) and H2020-MSCA-COFUND-2016 (DOC-FAM, grant agreement no. 754397). A.P. is grateful to the Spanish Ministry for Economy, Industry and Competitiveness Severo Ochoa Programme for Centres of Excellence in R&D (CEX2019-000917-S). D.F., C.C. and R.D. thank the French National Research Agency (STORE-EX Labex Project ANR-10-LABX-76-01) for financial support. K.R. and M.L. gratefully acknowledge the research funding by the Slovenian Research Agency (P1-0045, N1-0189). Alistore-European Research Institute is gratefully acknowledged for financial support through the postdoc grant to C.B. The SR-FTIR experiments were performed at MIRAS beamline at ALBA Synchrotron with the collaboration of ALBA staff. All DFT calculations were carried out at the Wroclaw Centre for Networking and Supercomputing within grant no. 346.

## Conflict of Interest

The authors declare no conflict of interest.

## Data Availability Statement

The data that support the findings of this study are available from the corresponding author upon reasonable request.

**Keywords:** boron-based adducts • calcium batteries • electrolyte additive • solid electrolyte interphase

- [1] A. Ponrouch, C. Frontera, F. Bardé, M. R. Palacín, *Nat. Mater.* **2015**, *15*, 169–172.
- [2] S. Biria, S. Pathreker, H. Li, I. D. Hosein, *ACS Appl. Energ. Mater.* **2019**, *2*, 7738–7743.
- [3] D. Wang, X. Gao, Y. Chen, L. Jin, C. Kuss, P. G. Bruce, *Nat. Mater.* **2018**, *17*, 16–20.
- [4] A. Shyamsunder, L. E. Blanc, A. Assoud, L. F. Nazar, *ACS Energy Lett.* **2019**, *4*, 2271–2276.

- [5] Z. Li, O. Fuhr, M. Fichtner, Z. Zhao-Karger, *Energy Environ. Sci.* **2019**, *12*, 3496–3501.
- [6] N. J. Leon, X. Xie, M. Yang, D. M. Driscoll, J. G. Connell, S. Kim, T. Seguin, J. T. Vaughan, M. Balasubramanian, K. A. Persson, C. Liao, *J. Phys. Chem. C* **2022**, *126*, 13579–13584.
- [7] S. Biria, S. Pathreker, F. S. Genier, H. Li, I. D. Hosein, *ACS Appl. Energ. Mater.* **2020**, *3*, 2310–2314.
- [8] K. Nielson, J. Luo, T. L. Liu, *Batteries & Supercaps* **2020**, *3*, 766–772.
- [9] Y. Zhao, A. Wang, L. Ren, X. Liu, J. Luo, *J. Energy Chem.* **2022**, *70*, 174–190.
- [10] J. D. Forero-Saboya, D. S. Tchitchekova, P. Johansson, M. R. Palacín, A. Ponrouch, *Adv. Mater. Interfaces* **2022**, *9*, 2101578.
- [11] J. Forero-Saboya, C. Davoisne, R. Dedryvère, I. Yousef, P. Canepa, A. Ponrouch, *Energy Environ. Sci.* **2020**, *13*, 3423–3431.
- [12] J. Forero-Saboya, C. Bodin, A. Ponrouch, *Electrochem. Commun.* **2021**, *124*, 106936.
- [13] L. Eisele, N. Laszcynski, M. Görg, M. Schneider, S. Burger, V. Radkte, B. Lucht, I. Krossing, *J. Electrochem. Soc.* **2020**, *167*, 080507.
- [14] J. D. Forero-Saboya, M. Lozinšek, A. Ponrouch, *J. Power Sources Adv.* **2020**, *6*, 100032.
- [15] L. A. J. Garvie, A. J. Craven, R. Brydson, *Am. Mineral.* **1995**, *80*, 1132–1144.
- [16] H. Sauer, R. Brydson, P. N. Rowley, W. Engel, J. M. Thomas, *Ultramicroscopy* **1993**, *49*, 198–209.
- [17] E. Quarez, E. Gautron, M. Paris, D. Gajan, J.-Y. Mevellec, *Inorg. Chem.* **2021**, *60*, 2406–2413.
- [18] M. Boniface, L. Quazuguel, J. Danet, D. Guyomard, P. Moreau, P. Bayle-Guillemaud, *Nano Lett.* **2016**, *16*, 7381–7388.
- [19] I. Rey, P. Johansson, J. Lindgren, J. C. Lassègues, J. Grondin, L. Servant, *J. Phys. Chem. A* **1998**, *102*, 3249–3258.
- [20] B. Fortunato, P. Mironi, G. Fini, *Spectrochim. Acta Part A* **1971**, *27*, 1917–1927.
- [21] L. Yang, M. M. Furczon, A. Xiao, B. L. Lucht, Z. Zhang, D. P. Abraham, *J. Power Sources* **2010**, *195*, 1698–1705.
- [22] D. M. Seo, D. Chalasani, B. S. Parimalam, R. Kadam, M. Nie, B. L. Lucht, *ECS Electrochem. Lett.* **2014**, *3*, A91.
- [23] C. E. Weir, R. A. Schroeder, *J. Res. Natl. Bur. Stand. Sect. A* **1964**, *68 A*, 465–487.
- [24] L. Eisele, N. Laszcynski, M. Schneider, B. Lucht, I. Krossing, *J. Electrochem. Soc.* **2020**, *167*, 060514.
- [25] J. S. Hartman, J. M. Miller, in *Adv. Inorg. Chem. Radiochem.*, Vol. 21 (Eds: H. J. Emeléus, A. G. Sharpe), Academic Press, **1978**, pp. 147–177.
- [26] X. Ou, R. Wallace, A. F. Janzen, *Can. J. Chem.* **1993**, *71*, 51–59.
- [27] D. A. Schulz, A. W. Searcy, *J. Phys. Chem.* **1963**, *67*, 103–106.
- [28] E. M. Erickson, E. Markevich, G. Salitra, D. Sharon, D. Hirshberg, E. de la Llave, I. Shterenberg, A. Rosenman, A. Frimer, D. Aurbach, *J. Electrochem. Soc.* **2015**, *162*, A2424.
- [29] R. Dugas, J. D. Forero-Saboya, A. Ponrouch, *Chem. Mater.* **2019**, *31*, 8613–8628.
- [30] R. F. Egerton, *Electron Energy-Loss Spectroscopy in the Electron Microscope*, Springer US, New York, **1996**.
- [31] L. Dupont, L. Laffont, S. Gruegeon, S. Laruelle, V. Bodenez, J.-M. Tarascon, *ECS Trans.* **2007**, *3*, 139–153.
- [32] Rigaku Oxford Diffraction, *CrysAlisPro* Software System, v. 1.171.41–64.123a and v. 1.171.42.57a, Rigaku Corporation, Wroclaw, Poland, **2022**.
- [33] O. V. Dolomanov, L. J. Bourhis, R. J. Gildea, J. A. K. Howard, H. Puschmann, *J. Appl. Crystallogr.* **2009**, *42*, 339–341.
- [34] L. Palatinus, G. Chapuis, *J. Appl. Crystallogr.* **2007**, *40*, 786–790.
- [35] L. Palatinus, S. J. Prathapa, S. van Smaalen, *J. Appl. Crystallogr.* **2012**, *45*, 575–580.
- [36] G. M. Sheldrick, *Acta Crystallogr.* **2015**, *C71*, 3–8.
- [37] K. Brandenburg, *Diamond – Crystal and Molecular Structure Visualization*, v. 3.1, Crystal Impact GbR, Bonn, Germany, **2005**.
- [38] R. I. Cooper, A. L. Thompson, D. J. Watkin, *J. Appl. Crystallogr.* **2010**, *43*, 1100–1107.
- [39] M. Lozinšek, H. P. A. Mercier, G. J. Schrobilgen, *Angew. Chem. Int. Ed.* **2021**, *60*, 8149–8156.

Manuscript received: September 30, 2022  
Revised manuscript received: October 12, 2022  
Accepted manuscript online: October 13, 2022  
Version of record online: November 8, 2022